High Thermoelectric Performance and Low Thermal Conductivity in $Cu_{2-y}S_{1/3}Se_{1/3}Te_{1/3}$ Liquid-like Materials with Nanoscale Mosaic Structures

Kunpeng Zhao[a,b], Chenxi Zhu[a,b], Pengfei Qiu[a], Anders Bank Blichfeld[c,d], Espen Eikeland[c,e], Dudi Ren[a], Bo B. Iversen[c], Fangfang Xu[a], Xun Shi[a,*], and Lidong Chen[a,*]

[a] State Key Laboratory of High Performance Ceramics and Superfine Microstructure, Shanghai Institute of Ceramics, Chinese Academy of Sciences, Shanghai 200050, China.
[b] University of Chinese Academy of Sciences, Beijing 100049, China.
[c] Centre for Materials Crystallography, Department of Chemistry and iNANO, Aarhus University, Langelandsgade 140, DK-8000 Aarhus C, Denmark.
[d] Department of Materials Science and Engineering, Norwegian University of Science and Technology, N-7491 Trondheim, Norway.
[e] Danish Technological Institute, Centre for Nano Production and Micro Analysis, DK-2630 Taastrup, Denmark
* Corresponding author. E-mail: xshi@mail.sic.ac.cn and cld@mail.sic.ac.cn

Abstract

Mosaic-crystal microstructure is one of the optimal strategies for decoupling and balancing thermal and electrical transport properties in thermoelectric materials. Herein, we successfully achieve the desired nanoscale mosaic structures in triple-component $Cu_{2-y}S_{1/3}Se_{1/3}Te_{1/3}$ solid solutions using Cu_2S, Cu_2Se, and Cu_2Te matrix compounds. They are solved in hexagonal structures with space group $R\bar{3}m$ by means of single crystal structural solution and Rietveld refinement. Electron backscatter diffraction measurements show that all the samples are polycrystalline compounds with the grain size in the range of micrometers. However, transmission electron microscopic study reveals that these microscale grains are quasi-single crystals consist of a variety of 10-30 nm mosaic grains. Each mosaic grain is a perfect crystal but titled or rotated with respect to others by a very small angle. In this case, excellent electrical transports are maintained but exceptional low thermal conductivity is achieved throughout the whole temperature range, which is attributed to the combined phonon scatterings by point defects, liquid-like copper ions, and lattice strains or interfaces of mosaic nanograins. Combining all these favorable factors, remarkably high thermoelectric performance is achieved in $Cu_{1.98}S_{1/3}Se_{1/3}Te_{1/3}$

with a maximum zT of 1.9 at 1000 K.

Keyword: thermoelectric, mosaic structure, solid solution, thermal conductivity, electrical conductivity

1. Introduction

Thermoelectric (TE) materials, which are capable of direct and reversible conversion between heat and electricity, have attracted widespread research interests due to their advantages of no moving parts, no mechanical or chemical processes involved, emission free, high durability, and reliability [1-5]. TE technology shows a great potential in a variety of applications such as spot cooling and power generation using waste heat [6]. The energy conversion efficiency is characterized by the dimensionless figure of merit, defined as $zT = S^2T/(\rho\kappa)$, where S, T, ρ, and κ are the Seebeck coefficient, absolute temperature, electrical resistivity, and total thermal conductivity (including the lattice contribution κ_L and the carrier contribution κ_c), respectively. The κ_L is considered the most decoupled parameter and the other parameters S, ρ, and κ_c, however, are strongly interrelated, which are determined by materials carrier concentrations and electronic structures [7]. Therefore, decoupling or balancing these parameters to synergistically optimize electrical and thermal transports for substantially improving TE performance is historically a long sought goal.

In the past two decades, tremendous exploratory efforts have been made to improve zTs [8-17]. High thermoelectric performance is usually reported in either single crystals or nano-materials, which are the two extreme crystallization regimes [16-19]. Single crystals have excellent electrical and thermal conductivities because of the absence of boundary or interface scatterings to electrons and phonons [17, 18]. In contrast, nano-materials usually have low electron and phonon conduction because of the effective electron and phonon scatterings on boundaries and interfaces [16, 19]. Recently, the unusual mosaic-crystal microstructure in nanoscale was proposed by He *et al.* to balance the electrical and thermal transports properties for much high zTs [9]. Mosaic crystal is a very special state with a high degree of perfection in lattice translations throughout the crystal [9, 20, 21]. It is composed of mosaic blocks with each block

being a perfect crystal but titled or rotated with respect to others by a fraction of arc. In contrast to ordinary polycrystals or nanocrystal materials, which have random orientations, a mosaic crystal has the blocks that exhibit a nearly identical orientation. Consequently, good electronic transport, similar to that in a single crystal, may be observed in a mosaic crystal because of the high lattice coherence. Meanwhile, small angle grain boundaries still show effective mis-orientation in scattering heat-conducting phonons, resulting in exceptional low κ_L [9]. Thus, the mosaic crystal structures, especially in nanoscale, can combine the characters of single crystals and nano-materials, which are very helpful for the improvement of TE performance.

In this work, we successfully achieved the desired nanoscale mosaic structure in triple-component solid solutions, i.e. $Cu_{2-y}S_{1/3}Se_{1/3}Te_{1/3}$ using the large atomic size mis-match between S, Se, and Te. The microscale quasi-single crystals consist of 10-30 nm mosaic grains lead to extremely low thermal conductivity and good electrical properties and thus high TE performance with a zT~ 1.9 at 1000 K in $Cu_{1.98}S_{1/3}Se_{1/3}Te_{1/3}$.

2. Experimental Details

2.1 Synthesis.

High quality crystalline ingots (~ 3.2 g) of $Cu_{2-y}S_{1/3}Se_{1/3}Te_{1/3}$ (y = 0, 0.02, or 0.03) were synthesized by a melting-annealing-sintering process. High purity elements Cu (shot, 99.999%, Alfa Aesar), S (shot, 99.999%, Alfa Aesar), Se (shot, 99.999%, Alfa Aesar), and Te (shot, 99.999%, Alfa Aesar) were loaded in Boron Nitride crucibles that sealed in a fused silica tube under vacuum. The tubes were firstly (100 K h^{-1}) raised to 1423 K and kept for 12 h, then slowly (7 K h^{-1}) cooled down to 1073 K and soaked at that temperature for 8 days, finally naturally cooled to room temperature. Small single crystals were extracted from the as-prepared polycrystalline ingot samples. The obtained ingots were crushed into powders and consolidated by spark plasma sintering (Sumitomo SPS-2040) at 873 K under a pressure of 65 MPa for 5 minutes. Electrically insulating and thermally conducting BN layers were sprayed onto the carbon foils and the inner sides of the graphite die before the SPS process in order to prohibit DC pulsed currents going through the powders.

2.2 Characterization.

Single-crystal (about 10 × 40 × 60 μm^3) X-ray diffraction (SCXRD) measurements were performed on a SuperNova diffractometer from Agilent Technologies using $Mo_{K\alpha}$ radiation (λ= 0.71073 Å). Diffracted intensities were collected on a CCD detector and the data were integrated and corrected for absorption using CrysAlisPro. The structure solution and refinement were carried out with SHELXT, using the Olex2 gui. Room-temperature powder X-ray diffraction (RT-PXRD) data was recorded using a Cu K_α (λ= 1.5406 Å) radiation on a Rigaku Rint 2000 diffractometer. Full profile refinements by Rietveld analysis were carried out for $Cu_{2-y}S_{1/3}Se_{1/3}Te_{1/3}$ samples using the program Full-Prof. The electron backscatter diffraction (EBSD) measurement was carried out on field emission scanning electron microscopy (FESEM, Magellan-400) equipped with energy dispersive X-ray analysis (EDS, Horiba 250). The ultrathin sectioning method has been used to prepare samples for TEM observations. The thin sectioned samples with a thickness of 35 nm have been obtained on a LEICA EM UC7 microtome by using a diamond knife at a cutting speed of 0.4 mm s^{-1}. The sectioned sample was floated on the water and then transferred onto the Mo grid. The sound speed data were obtained by use of ultrasonic measurement system UMS-100 with shear wave transducers of 5 MHz and longitudinal wave transducers of 10 MHz. The electrical resistivity (ρ) and the Seebeck coefficient (S) at 300–1000 K were measured using ZEM-3 (ULVAC Co. Ltd) apparatus under a helium atmosphere. The thermal diffusivity (D) was measured in an argon atmosphere using a laser flash method (LFA 457, Netzsch Co. Ltd). The specific heat (C_p) was determined by differential scanning calorimetric using Netzsch DSC 404F3. The density (d) was measured using the Archimedes method. The total thermal conductivity (κ) was calculated according to the relationship $\kappa = dC_pD$. Measurment uncertainties in the electrical resistivity, Seebeck coefficient, and thermal diffusivity were 4-9%, 4%, and 5-10%, respectively [22]. The Hall coefficient (R_H) at 300 K was measured using a physical properties measurement system (PPMS-9, Quantum Design, USA) with a magnetic field from -3 to 3 T. The hole concentration (p) was calculated using $p = 1/R_He$, where e is the elementary charge. Hall carrier mobility (μ_H) was calculated according to the relation $\mu_H = R_H/\rho$.

3. Results and Discussion

3.1 Crystal Structure

The single-crystal X-ray diffraction measurements have been performed to solve the crystal

structure of $Cu_2S_{1/3}Se_{1/3}Te_{1/3}$ compound at 100 K. The details of data collection and crystal structure refinements are given in Table S1. The structure was solved by intrinsic phasing resulting in the hexagonal structure with space group $P6_3/mmc$, which is the same as the intermediate temperature phase of Cu_2S and the room temperature phases of $Cu_2Se_{1-x}S_x$ and $Cu_2S_{1-x}Te_x$ solid solutions [9, 23-25]. As depicted in **Figure 1a**, the hexagonal unit cell of $Cu_2S_{1/3}Se_{1/3}Te_{1/3}$ contains two $Cu_2S_{1/3}Se_{1/3}Te_{1/3}$ formula units with cell parameters a = 4.052(2) Å and c = 6.849(6) Å. It has one shared S/Se/Te (2c) and two different kinds of copper (Cu1: 2b & Cu2: 12k) Wyckoff sites. The disordered S/Se/Te distributions indicate that the three matrix Cu_2X (X= S, Se, Te) compounds are completely miscible in the studied composition range. The Se/S/Te and Cu1 atoms form hexagon ring layers stacked along the c-axis. The Cu2 sites, being split into three equivalent positions (Cu2a, Cu2b, and Cu2c), are situated above and below the center of the hexagon rings. The S/Se/Te sites are fully occupied, whereas the Cu sites are partially occupied. Totally, there are two Cu cations distributed over 14 crystallographic sites per unit cell. Thus there are many empty Cu positions that provide jumping channels for Cu ions (Figure 1b).

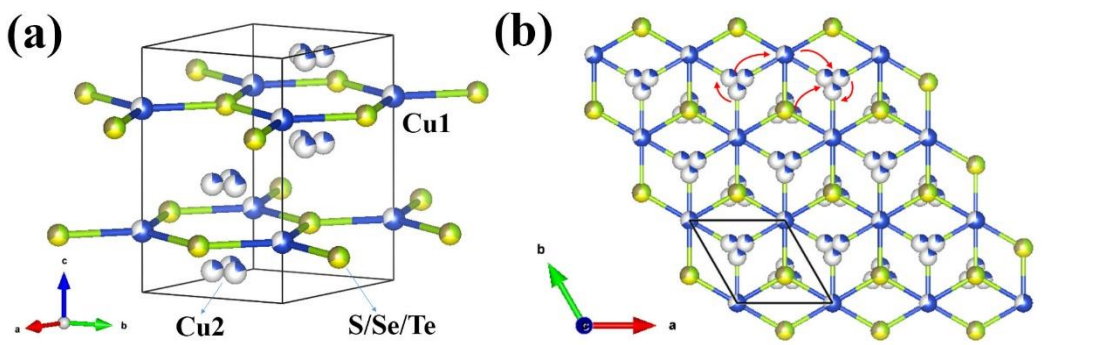

Figure 1. Hexagonal structure of $Cu_2S_{1/3}Se_{1/3}Te_{1/3}$ at 100 K with a space group of $P6_3/mmc$. **(a)** Unit cell with one shared S/Se/Te site and two Cu sites (Cu1 and Cu2). For simplicity, only the bonds between S/Se/Te and Cu1 (with the interatomic distances of ≤2.3467 Å) are shown. **(b)** Projected plane representation of the crystal structure along the [001] direction. The red arrows indicate that the Cu ions can travel among different Cu sites. The atomic site occupancy is indicated by partial coloring of the atoms.

The X-ray diffraction patterns measured on powder $Cu_{2-y}S_{1/3}Se_{1/3}Te_{1/3}$ (y = 0, 0.02, or 0.03) samples are depicted in **Figure 2a**. All diffraction peaks of $Cu_2S_{1/3}Se_{1/3}Te_{1/3}$, $Cu_{1.98}S_{1/3}Se_{1/3}Te_{1/3}$,

and $Cu_{1.97}S_{1/3}Se_{1/3}Te_{1/3}$ are clearly indexed by the new hexagonal structure described above. The very similar diffractograms of these three samples suggest that a little Cu deficiency has limited effect on the crystal symmetry. This is different from the cases in binary $Cu_{2-y}X$ (X= S, Se, and Te) matrix compounds and $Cu_{2-y}Se_{0.5}S_{0.5}$ solid solutions [25-28], wherein the crystal structures are obviously affected by Cu deficiency. An exemplary Rietveld refined pattern for $Cu_2S_{1/3}Se_{1/3}Te_{1/3}$ is shown in Figure 2b with the difference profile shown below the pattern. The good quality factors and low residuals in the profile indicate good pattern fitting, which further confirms the correction of our crystal model obtained from the single-crystal structural solution. With the increase of temperature, $Cu_{2-y}S_{1/3}Se_{1/3}Te_{1/3}$ materials transform into cubic structure at around 700 K, as demonstrated by the DSC and HT-XRD measurements (Figure S2).

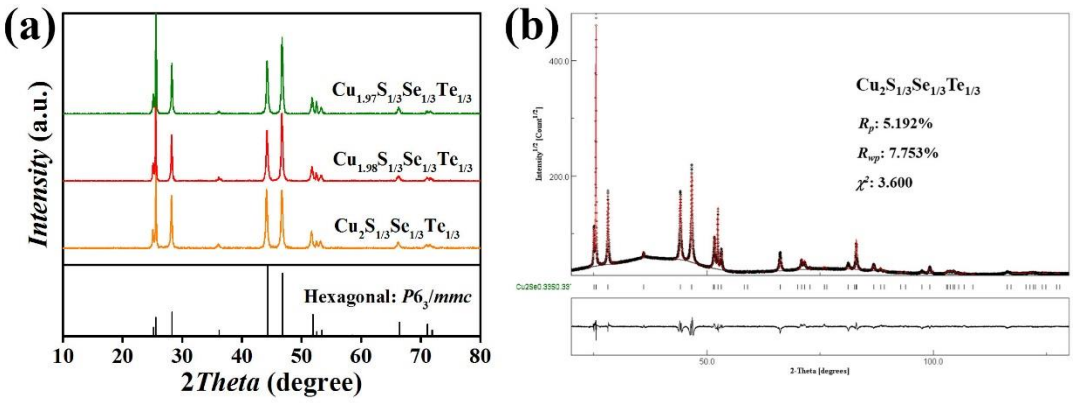

Figure 2. (a) Powder X-ray diffraction patterns for $Cu_{2-y}S_{1/3}Se_{1/3}Te_{1/3}$ (y = 0, 0.02, or 0.03) at room temperature. **(b)** Rietveld refinements for $Cu_2S_{1/3}Se_{1/3}Te_{1/3}$ sample and the overlaid calculated pattern (dashed line) with difference profile below.

3.2 Micro/nano-structures

We investigated the micro/nano-structural features using elemental energy dispersive spectroscopy (EDS), electron backscatter diffraction (EBSD) and transmission electron microscopy (TEM) techniques. The elemental mapping displays a homogeneous distribution of all elements across the sintered pellet, which further confirms the pure and uniform nature of solid solutions even after sintering. The actual compositions were determined by EDS on 10 randomly selected locations (see Table S1 and Table S2). We found the average actual compositions for $Cu_{2-y}S_{1/3}Se_{1/3}Te_{1/3}$ samples are very close to the nominal compositions. The inverse pole figure

(IPF) orientation map (Figure 3b), obtained by EBSD, reveals the shape, size, and distribution of the crystal grains. Most of the grains are in the range of several microns (Figure 3c). Each grain usually is a single crystal. However, the case is different in current study. The transmission electron microscopy (TEM) analyses are performed on the ultrathin sectioned samples (see Figure 4a) to gain insight into details of the nanoscales in the lattice and atomic levels. Figure 4b shows a near-perfect single-crystal type selected-area electron diffraction (SAED) pattern of [0001] zone axis of circle-framed area in Figure 4a. The Bragg-diffracted electrons form arcing short bars rather than traditional sharp dots, suggesting the presence of tiny degree of mis-orientation. This is a typical character of mosaic crystal as described before [9]. Magnified bright/dark-field images further confirm these mosaic features, as shown in Figure 4c, d and e. The rotation around and tilting off [0001] axis of different nano-crystals leads to the formation of inhomogeneous particle-shape contrast in dark-field image. The pseudo-single crystal consists of many nano-crystals with the size of 10-30 nanometers. High resolution electron microscopy analysis is also performed in order to further examine the mosaic character. The fast Fourier transform (FFT) diffractogram of the square-framed area in Figure 4f shows still a [0001] single-crystal pattern. However, several nano-crystals can be identified from the picture. The FFT patterns of each area possessing independent intensities represent to the small rotation or tilting of these nano-crystals with respect to each other. The above structural analysis demonstrates that a typical nanoscale mosaic microstructure in poly-crystalline grains is obtained. The special mosaic structure, in the present case, is mainly caused by the large atomic size mismatch between S, Se, and Te. Thus the stability is quite good and the mosaic micro-structures are maintained after high temperature heat treatment [9], which is strongly supported by good reproducibility in electrical conductivity and Seebeck coefficient after heat cycling tests (Fig. S4).

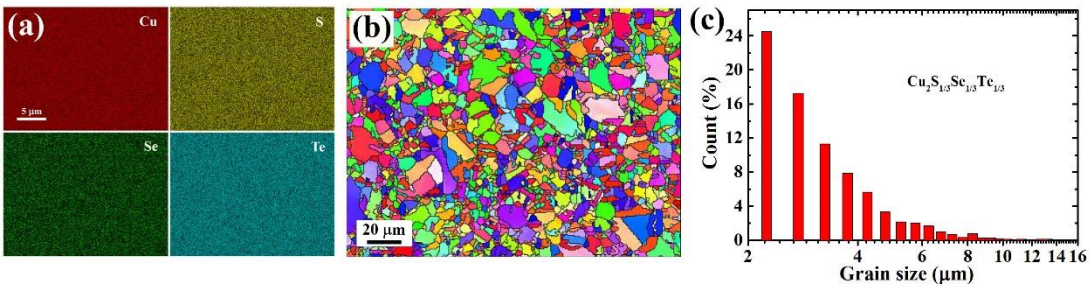

Figure 3. (a) Elemental energy dispersive spectroscopy (EDS) mapping for $Cu_2S_{1/3}Se_{1/3}Te_{1/3}$. **(b)**

Inverse pole figure (IPF) orientation map obtained from electron backscatter diffraction (EBSD) measurement. **(c)** Size distribution histogram of the grains in Figure 3b for $Cu_2S_{1/3}Se_{1/3}Te_{1/3}$ sample.

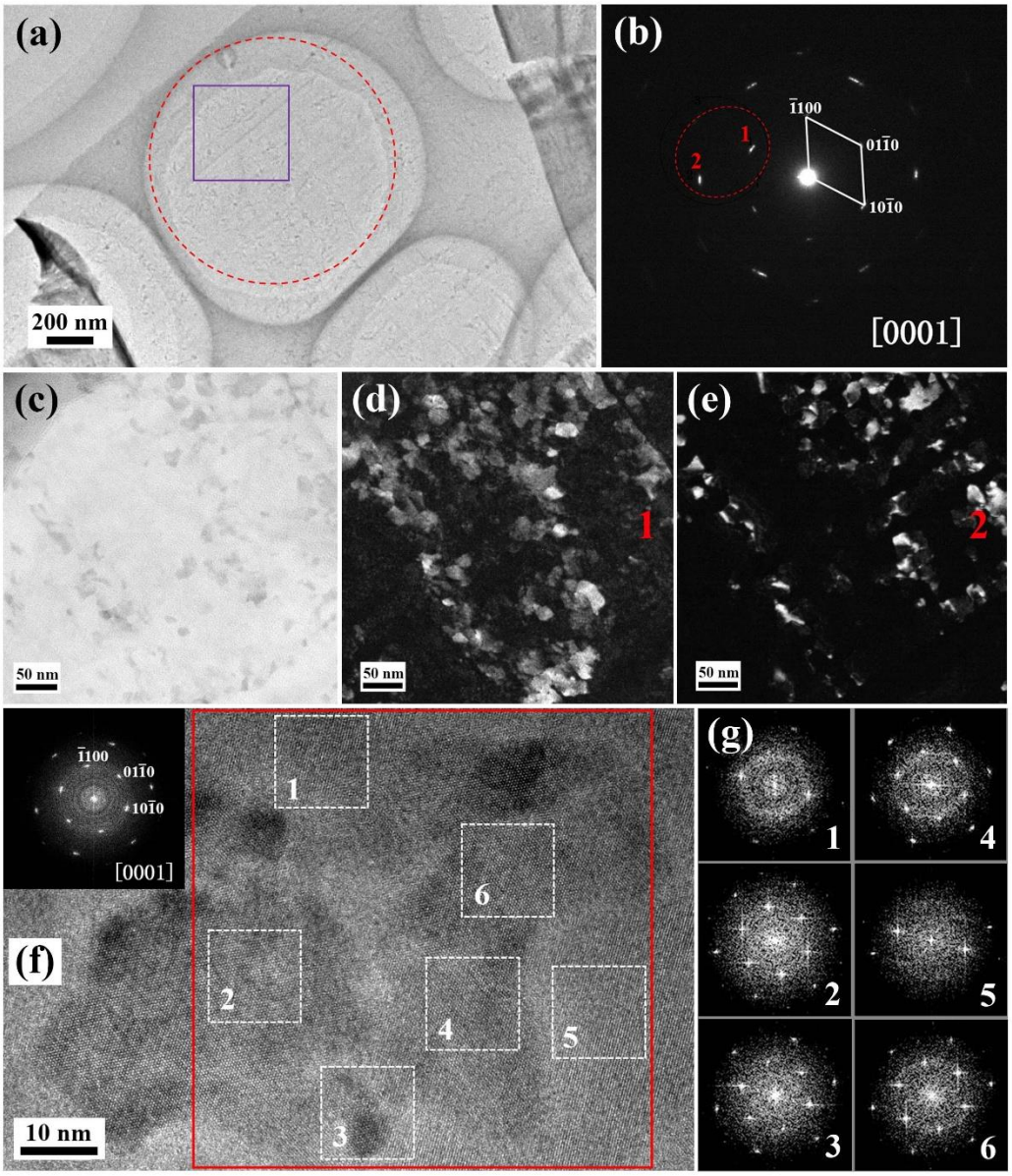

Figure 4. TEM and HRTEM analyses of the mosaic structure in $Cu_2S_{1/3}Se_{1/3}Te_{1/3}$. **(a)** Bright-field image of the ultra-thin sectioned sample. **(b)** Electron diffraction pattern of a large area (circumvented by a red circle in (a)) indicating a 'quasi-single crystalline' structure. **(c, d, e)** Bright-field and dark-field images of the purple framed area in (a). Dark-field images d and e are obtained using the diffraction spots 1 and 2 in (b), respectively. **(f)** HRTEM image and FFT diffractogram of the red framed area. **(g)** FFT diffractograms of selected areas in (f) labeled as 1, 2,

3, 4, 5, and 6, respectively. The nanocrystallites show nearly identical diffractograms except for variations in the brightness of different reflections that correspond to a slight misorientation with respect to each other.

3.3 Electrical Transport Properties.

Transport property measurements were performed on the highly dense SPS sintered polycrystalline $Cu_{2-y}S_{1/3}Se_{1/3}Te_{1/3}$ (y= 0, 0.02, or 0.03) samples and the measured TE properties are showed in **Figure 5**. The data of Cu_2S, Cu_2Se, and Cu_2Te matrix compounds are also included for comparison [10, 29, 30]. The temperature dependent Hall carrier concentrations, *p*, of all samples are positive, indicating the p-type conduction in this system. At room temperature, the *p* value of $Cu_2S_{1/3}Se_{1/3}Te_{1/3}$ is around 6.6×10^{20} cm^{-3}, which is lower than that of Cu_2Te but higher than those of Cu_2S and Cu_2Se matrix compounds. With increasing copper deficiency from $Cu_2S_{1/3}Se_{1/3}Te_{1/3}$ to $Cu_{1.97}S_{1/3}Se_{1/3}Te_{1/3}$, the room temperature carrier concentration is significantly increased from 6.6×10^{20} cm^{-3} to 1.7×10^{21} cm^{-3}. Such increased trend in hole concentration is also observed in $Cu_{2-y}X$ (X= S, Se, and Te) matrix compounds [26, 27] and $Cu_{2-y}Se_{0.5}S_{0.5}$ solid solution [25], which is contributed by the excess holes from Cu vacancies. The electrical resistivity ρ for all $Cu_{2-y}S_{1/3}Se_{1/3}Te_{1/3}$ samples shows two different temperature dependencies in the temperature range from 300 K to 1000 K, which are attributed to the structural transformations discussed above. Above their respective phase transition temperatures (600-700K), the ρ is monotonically increased with the increase in temperature, showing typical heavily-doped semiconducting behavior. Owing to the improved carrier concentration in Cu deficient samples, both electrical resistivity and Seebeck coefficient are decreased over the whole temperature range compared to that of stoichiometric $Cu_2S_{1/3}Se_{1/3}Te_{1/3}$. The overall trend in Seebeck coefficient *S* is increased with increasing temperature, except small discontinuous jumps around 650 K because of the structural transformations. The *S* values of $Cu_{2-y}S_{1/3}Se_{1/3}Te_{1/3}$ solid solutions are comparable to the *S* of Cu_2Se but lie between those of Cu_2Te and Cu_2S matrix compounds over the entire temperature range. The positive sign of the Seebeck coefficient further confirms that holes are the dominant charge carriers, which agrees with the Hall measurement. In addition, we have run the cycling tests on sample $Cu_{1.97}Se_{1/3}Se_{1/3}Te_{1/3}$, which is shown in Figure S4. Up to 850 K, both electrical conductivity and Seebeck coefficients are almost the same.

The power factors calculated from the formula PFs= S^2/ρ for all samples are shown in Figure 5d. As a result of the reduced ρ and α values, the PF values of $Cu_{2-y}S_{1/3}Se_{1/3}Te_{1/3}$ show a monotonously increase with increasing the Cu vacancies, especially at high temperatures. The room temperature PFs for $Cu_{2-y}S_{1/3}Se_{1/3}Te_{1/3}$ solid solutions, as well as Cu_2S and Cu_2Te matrix compounds, are rather small, with the values around 1 μW cm^{-1} K^{-1}. They are obviously lower than that of Cu_2Se. Nevertheless, the PFs are greatly improved at elevated temperatures. The maximum PF, around 11.2 μW cm^{-1} K^{-2} at 1000 K, has been obtained for $Cu_{1.97}S_{1/3}Se_{1/3}Te_{1/3}$, which is comparable to that of Cu_2Se and higher than those of Cu_2S and Cu_2Te matrix compounds at the same temperature.

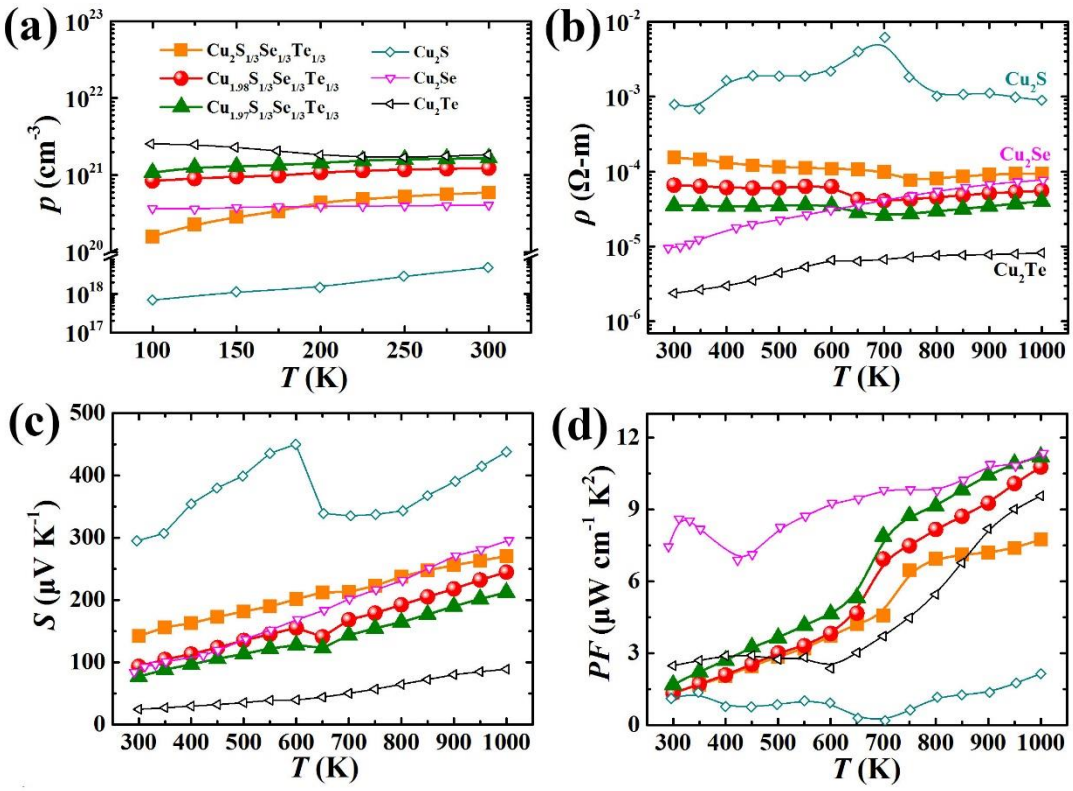

Figure 5. Temperature dependent electrical transport properties of $Cu_{2-y}S_{1/3}Se_{1/3}Te_{1/3}$ (y= 0, 0.02, or 0.03). **(a)** Carrier concentration p, **(b)** electrical resistivity ρ, **(c)** Seebeck coefficient S, and **(d)** power factor PF. The data of Cu_2S, Cu_2Se and Cu_2Te are also included for comparison [10, 29, 30].

Combining the single parabolic band (SPB) model under the relaxation time approximation, the Hall carrier concentration p and Seebeck coefficient S can be correlated as follows [31, 32]:

$$\alpha = \frac{k_B}{e}\left[\frac{(2+\lambda)F_{\lambda+1}(\eta)}{(1+\lambda)F_{\lambda}(\eta)} - \eta\right] \quad ,(1)$$

$$p = \frac{1}{2\pi^2}\left(\frac{2m^* k_B T}{\hbar^2}\right)^{3/2}\frac{F_{1/2}(\eta)}{r_H} \quad ,(2)$$

where k_B is the Boltzmann constant, e is the elementary charge, λ is the scattering factor with a value of 0 for combined acoustic phonon scattering and alloy scattering, and η (=E_F/k_BT) is the reduced Fermi energy. The Fermi integrals are given by $F_m(\eta) = \int_0^\infty \frac{x^m dx}{1+\exp(x-\eta)}$, where x is the reduced carrier energy, $\hbar$ is the reduced Planck constant and r_H is the Hall factor given by $r_H = \frac{3}{4}\frac{F_{1/2}(\eta)F_{-1/2}(\eta)}{{F_0}^2(\eta)}$. Assuming that carrier scattering is dominated by a combination (λ= 0) of acoustic phonon scattering and alloy scattering at room temperature, the Pisarenko plots (α *vs*. p) under different effective masses are calculated according to the above expressions and shown in **Figure 6**. For comparison, the reported S *vs.* p experimental data of $Cu_{2-y}X$ (X= S, Se, and Te) matrix compounds [10, 29, 30], $Cu_2Se_{1-x}S_x$ [24] and $Cu_2S_{1-x}Te_x$ [9] solid solutions are also given here. Clearly, the experimental S data for Cu_2X (X= S, Se, and Te) matrix compounds and $Cu_2Se_{1-x}S_x$ solid solutions fall right in the yellow area with the effective masses m^* range from 1.0 to 2.3 m_e (m_e is the free electron mass). However, the room temperature S values of mosaic crystals, $Cu_2S_{1-x}Te_x$ and $Cu_{2-y}S_{1/3}Se_{1/3}Te_{1/3}$, reside far above the yellow area. Much high effective masses m^* of 4.5 and 5.6 m_e are obtained for $Cu_2S_{1-x}Te_x$ and $Cu_{2-y}S_{1/3}Se_{1/3}Te_{1/3}$, respectively. The widely dispersed mosaic nanograins in $Cu_2S_{1-x}Te_x$ and $Cu_{2-y}S_{1/3}Se_{1/3}Te_{1/3}$ are responsible for this unusual behavior. This originates probably due to energy dependent scattering of carriers, leading to an energy filtering effect that enhances the Seebeck coefficient [33]. Similar trend was also observed in Pt-Sb_2Te_3 [34] and PbTe nanocomposites [35].

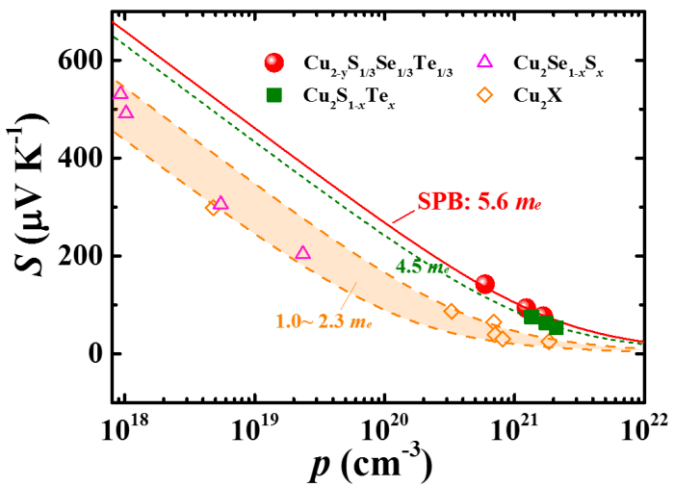

Figure 6. Calculated Pisarenko plots (Seebeck coefficients as a function of carrier concentration) and experimental *S vs. p* values at 300 K. For comparison, the reported *S vs. p* experimental data of $Cu_{2-y}X$ (X= S, Se, and Te) matrix compounds [10, 29, 30], $Cu_2Se_{1-x}S_x$ [24] and $Cu_2S_{1-x}Te_x$ [9] solid solutions are also given.

3.4 Thermal Transport Properties.

Figure 7d presents the total thermal conductivity κ as a function of temperature for $Cu_{2-y}S_{1/3}Se_{1/3}Te_{1/3}$ solid solutions. The reported data of Cu_2S, Cu_2Se and Cu_2Te are also included for comparison [10, 29, 30]. Similar to the electrical transport properties, the κ of $Cu_{2-y}S_{1/3}Se_{1/3}Te_{1/3}$ solid solutions show two temperature dependencies in the temperature range from 300 K to 1000 K due to the phase transitions. At low temperatures, extremely low κ values around 0.4 W m^{-1} K^{-1} are obtained for $Cu_{2-y}S_{1/3}Se_{1/3}Te_{1/3}$, which is comparable to that of Cu_2S but lower than those in Cu_2Se and Cu_2Te. At high temperatures, the κ of solid solutions range from 0.5 W m^{-1} K^{-1} to 0.8 W m^{-1} K^{-1}, in between those of Cu_2S and Cu_2Se matrix compounds. The lattice thermal conductivity (κ_L) can be calculated through subtracting the charge carrier component (κ_c) from the total thermal conductivity (κ) via the relationship $\kappa_c = LT/\rho$, where L is the Lorenz number (see Figure S2) extracted on the basis of the approximately reduced chemical potential [36]. Due to the relatively high electrical resistivity in $Cu_2S_{1/3}Se_{1/3}Te_{1/3}$, the subtracted carrier contribution κ_c to the thermal conductivity is less than 0.2 W m^{-1} K^{-1} (see Figure 7b). With increasing content of Cu vacancies, κ_c increases gradually because of the increased hole concentrations. The lattice thermal conductivity for all solid solutions are extremely low with the largest κ_L values not exceeding 0.42 W m^{-1} K^{-1} from 300 K to 1000 K. Such low κ_L values are

comparable to that of Cu_2S but much lower than that of Cu_2Se, as shown in **Figure 7c**. In addition, all the samples show a weak temperature dependent behavior in κ_L from room temperature to high temperatures. This is in contrast to the strong temperature dependency of normal crystalline compounds, which usually follows a T^{-1} trend at high temperatures due to the dominant phonon Umklapp-scattering process.

In the context of a random walk between Einstein oscillators of varying sizes, the limit for the minimum lattice thermal conductivity κ_{min} of normal solids can be expressed as the following sum of three Debye integrals (Cahill's formulation) [37]:

$$\kappa_{min} = \left(\frac{\pi}{6}\right)^{1/3} k_B n^{2/3} \sum_i v_i \left(\frac{T}{\Theta_i}\right)^2 \int_0^{\Theta_i/T} \frac{x^3 e^x}{(e^x - 1)^2} dx \qquad .(3)$$

The sum is taken over the three sound modes (one longitudinal v_l and two transverse v_t) with speeds of sound v_i. Θ_i $(= v_i(\hbar/k_B)(6\pi^2 n)^{1/3})$ is the cutoff frequency for each polarization, and n is the number density of atoms. Ultrasonic measurements performed on $Cu_2S_{1/3}Se_{1/3}Te_{1/3}$ show that the longitudinal v_l and transverse sound velocities v_t are 3100 and 1400 m s^{-1}, respectively (see Figure S3). The temperature dependence of the calculated minimum thermal conductivity κ_{min} for $Cu_2S_{1/3}Se_{1/3}Te_{1/3}$ is shown in Figure 7c (red dashed line). Interestingly, the calculated κ_{min} value (~0.49 W m^{-1} K^{-1}) is higher than the measured lattice thermal conductivity over the whole temperature range, which is in accordance with observations made on the other liquid-like compounds Cu_2Se, Ag_8SnSe_6, and Cu_7PSe_6 [10, 38, 39]. The abnormal low lattice thermal conductivity in these superionic conductors can be attributed to their special 'PLEC' character. Part of the transverse phonons with frequency lower than cut-off frequency would not take part in heat propagation due to the presence of liquid-like Cu ions [10]. Thus, a fraction of the heat propagating modes has to be removed when using Cahill's formulation to calculate the κ_{min} for liquid-like materials. For instance, in order to bring the κ_{min} calculated here for $Cu_2S_{1/3}Se_{1/3}Te_{1/3}$ in the range of the measured κ_L values, half of the transverse modes would have to be removed, as shown in Figure 7c.

Figure 7d shows the low temperatures (3-300 K) lattice thermal conductivity of $Cu_2S_{1/3}Se_{1/3}Te_{1/3}$ compound compared to that of crystalline Cu_2S, Cu_2Se, In_4Se_3, $Ba_8Ga_{16}Ge_{30}$, and

amorphous α-SiO_2 [9, 37, 40]. In general, a strong "hump" shape is normally observed in κ_L of crystalline materials such as Cu_2S, In_4Se_3, and $Ba_8Ga_{16}Ge_{30}$ compounds [41, 42]. While for amorphous materials, the temperature dependence of κ_L usually show a characteristic "plateau" phenomenon at 2-20 K [43]. However, being different from either crystalline or amorphous materials, the κ_L of $Cu_2S_{1/3}Se_{1/3}Te_{1/3}$ is monotonously increased with increasing temperatures without a "hump" or "plateau". Furthermore, extremely low κ_L values are also observed at low temperatures for $Cu_2S_{1/3}Se_{1/3}Te_{1/3}$. For example, the κ_L of $Cu_2S_{1/3}Se_{1/3}Te_{1/3}$ at 10 K is only 0.03 W m^{-1} K^{-1}, which is 8 times lower than that in amorphous α-SiO_2 and 10-70 times smaller than that in crystalline Cu_2S and $Ba_8Ga_{16}Ge_{30}$. This indicates the phonon mean free path of $Cu_2S_{1/3}Se_{1/3}Te_{1/3}$ at low temperatures is far less than that in typical crystalline compounds or amorphous materials. In addition to the strong phonon scattering by liquid-like ions and point defects, the extremely low κ_L value for $Cu_2S_{1/3}Se_{1/3}Te_{1/3}$ in the present case should be associated with its unusual mosaic structures discussed above. Mosaic crystals contain a number of small angle tilt or rotate boundaries that will introduce long range disorder for thermal phonons, leading to the exceptionally low lattice thermal conductivity observed in Figure 7d.

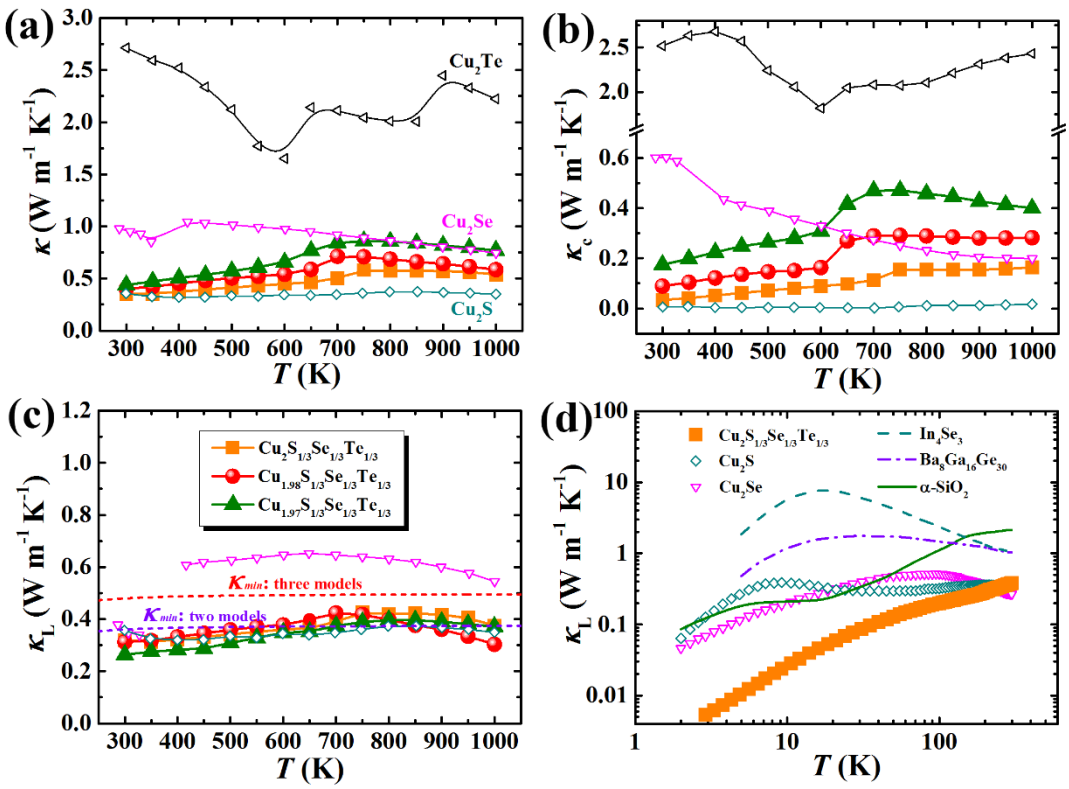

Figure 7. Temperature dependent thermal transport properties of $Cu_{2-y}S_{1/3}Se_{1/3}Te_{1/3}$ (y= 0, 0.02, or 0.03). **(a)** Total thermal conductivity κ, **(b)** carrier thermal conductivity κ_c, **(c)** lattice thermal conductivity κ_L (300-1000K), and **(d)** low temperature lattice thermal conductivity κ_L (2-300K). The red dashed line in (c) represents the minimum lattice thermal conductivity (κ_{min}) in $Cu_2S_{1/3}Se_{1/3}Te_{1/3}$ estimated by the Cahill's formula with three models (one longitudinal model + two transverse models), while the violet dashed line is calculated using two models (one longitudinal model + one transverse model). The reported data of Cu_2S, Cu_2Se, Cu_2Te, In_4Se_3, $Ba_8Ga_{16}Ge_{30}$, and amorphous α-SiO_2 are also included for comparison [10, 29, 30]. The κ_L data for Cu_2Te is not shown because the electronic contribution dominates the total thermal conductivity, leading to large error bars for the estimated lattice thermal conductivity.

3.5 Figure of Merit.

By combining the electrical and thermal transport properties, we determined the temperature dependent TE Figure of merit zT (Figure 5f). Similar to the behavior of PFs, the zT values of $Cu_2Se_{1-x}S_x$ solid solutions are increased with increasing temperature with maximum values of 1.5, 1.9, and 1.5 for $Cu_2S_{1/3}Se_{1/3}Te_{1/3}$, $Cu_{1.98}S_{1/3}Se_{1/3}Te_{1/3}$, and $Cu_{1.97}S_{1/3}Se_{1/3}Te_{1/3}$, respectively. These high zT values can be attributed to the moderate power factor and the extremely low lattice thermal conductivity. The strategy of nanoscale mosaicity provides a feasible route to decouple and balance thermal and electrical transport properties. It can also easily couple with other as-established optimization approaches such as band-structure engineering or element doping to further optimize thermoelectric performance. Beyond bulk materials, mosaic microstructures are expected to more easily form in thin films because thin films can tolerate large lattice strains and be cooled fast during material fabrication. This has been well demonstrated in the thin films of nitride semiconductors [44, 45].

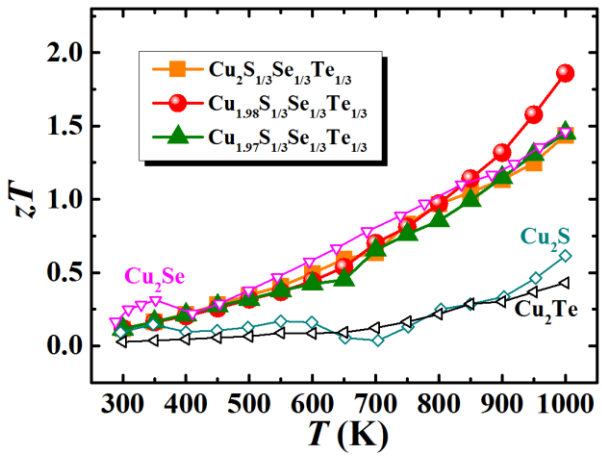

Figure 8. Temperature dependence of *zT* values for $Cu_{2-y}S_{1/3}Se_{1/3}Te_{1/3}$ (y= 0, 0.02, or 0.03) solid solutions. The reported data of Cu_2S, Cu_2Se, and Cu_2Te matrix are also included for comparison [10, 29, 30].

4. Conclusions

In summary, a series of $Cu_{2-y}S_{1/3}Se_{1/3}Te_{1/3}$ (y= 0, 0.02, or 0.03) solid solutions have been fabricated and their crystal structure, microstructures, and thermoelectric properties are systematically studied. The $Cu_{2-y}S_{1/3}Se_{1/3}Te_{1/3}$ compounds are solved in hexagonal structure with all element homogeneously distributed, indicating a perfect solid solution. Very special and unique nanoscale mosaic structures are observed. The mosaic nano-grains are around 10-30 nm with each other titled or rotated by a tiny angle, which can significantly lower the lattice thermal conductivity. By combing the strong phonon scattering from point defects, an overall ultralow lattice thermal conductivity with values less than 0.4 W m^{-1} K^{-1} is observed in $Cu_{2-y}S_{1/3}Se_{1/3}Te_{1/3}$. Furthermore, the electrical transports of $Cu_{2-y}S_{1/3}Se_{1/3}Te_{1/3}$ are well maintained due to the nearly identical orientated mosaic blocks. In consequence, a high *zT* value of 1.9 is achieved at 1000 K for $Cu_{1.98}S_{1/3}Se_{1/3}Te_{1/3}$, which is higher than Cu_2X matrix compounds. This strategy is expected to be easily applied in conjunction with existing successful approaches such as band-structure engineering to further enhance the thermoelectric performance.

Appendix A. Supplementary material

Supplementary data associated with this article can be found in the online version at http://dx.doi.

Acknowledgements

This work was supported by National Basic Research Program of China (973-program) under Project No. 2013CB632501, National Natural Science Foundation of China (NSFC) under the No. 51472262, Key Research Program of Chinese Academy of Sciences (Grant No. KGZD-EW-T06),

and Shanghai Government (16520721400 and 16XD1403900). B.B. Iversen thanks for the support by the Danish National Research Foundation (Center for Materials Crystallography, DNRF93), and the Danish Center for Synchrotron and Neutron Research (Danscatt). F.X. thanks National Natural Science Foundation of China (NSFC) for funding under Project No. 51672296.

References

[1] W. Liu, X. Yan, G. Chen, Z. Ren, Recent advances in thermoelectric nanocomposites, Nano Energy, 1 (2012) 42-56.

[2] G. Tan, L.D. Zhao, M.G. Kanatzidis, Rationally Designing High-Performance Bulk Thermoelectric Materials, Chem Rev, 116 (2016) 12123-12149.

[3] W.G. Zeier, A. Zevalkink, Z.M. Gibbs, G. Hautier, M.G. Kanatzidis, G.J. Snyder, Thinking Like a Chemist: Intuition in Thermoelectric Materials, Angewandte Chemie International Edition, 55 (2016) 6826-6841.

[4] X. Shi, L. Chen, C. Uher, Recent advances in high-performance bulk thermoelectric materials, International Materials Reviews, 61 (2016) 379-415.

[5] X. Su, P. Wei, H. Li, W. Liu, Y. Yan, P. Li, C. Su, C. Xie, W. Zhao, P. Zhai, Q. Zhang, X. Tang, C. Uher, Multi-Scale Microstructural Thermoelectric Materials: Transport Behavior, Non-Equilibrium Preparation, and Applications, Adv Mater, 29 (2017) 1602013.

[6] X. Shi, L. Chen, Thermoelectric materials step up, Nature Materials, 15 (2016) 691-692.

[7] Z. Li, C. Xiao, H. Zhu, Y. Xie, Defect Chemistry for Thermoelectric Materials, Journal of the American Chemical Society, 138 (2016) 14810-14819.

[8] Y. Pei, X. Shi, A. LaLonde, H. Wang, L. Chen, G.J. Snyder, Convergence of electronic bands for high performance bulk thermoelectrics, Nature, 473 (2011) 66-69.

[9] Y. He, P. Lu, X. Shi, F. Xu, T. Zhang, G.J. Snyder, C. Uher, L. Chen, Ultrahigh Thermoelectric Performance in Mosaic Crystals, Adv Mater, 27 (2015) 3639-3644.

[10] H. Liu, X. Shi, F. Xu, L. Zhang, W. Zhang, L. Chen, Q. Li, C. Uher, T. Day, G.J. Snyder, Copper ion liquid-like thermoelectrics, Nature Materials, 11 (2012) 422-425.

[11] A.I. Hochbaum, R. Chen, R.D. Delgado, W. Liang, E.C. Garnett, M. Najarian, A. Majumdar, P. Yang, Enhanced thermoelectric performance of rough silicon nanowires, Nature, 451 (2008) 163-167.

[12] W. Zhao, Z. Liu, P. Wei, Q. Zhang, W. Zhu, X. Su, X. Tang, J. Yang, Y. Liu, J. Shi, Magnetoelectric interaction and transport behaviours in magnetic nanocomposite thermoelectric materials, Nature nanotechnology, 12 (2016) 55-60.

[13] C. Fu, S. Bai, Y. Liu, Y. Tang, L. Chen, X. Zhao, T. Zhu, Realizing high figure of merit in heavy-band p-type half-Heusler thermoelectric materials, Nature Communications, 6 (2015) 8144.

[14] K. Zhao, A.B. Blichfeld, H. Chen, Q. Song, T. Zhang, C. Zhu, D. Ren, R. Hanus, P. Qiu, B.B. Iversen, F. Xu, G.J. Snyder, X. Shi, L. Chen, Enhanced Thermoelectric Performance through Tuning Bonding Energy in $Cu_2Se_{1-x}S_x$ Liquid-like Materials, Chemistry of Materials, 29 (2017) 6367-6377.

[15] H. Alam, S. Ramakrishna, A review on the enhancement of figure of merit from bulk to nano-thermoelectric materials, Nano Energy, 2 (2013) 190-212.

[16] K. Biswas, J. He, I.D. Blum, C.I. Wu, T.P. Hogan, D.N. Seidman, V.P. Dravid, M.G. Kanatzidis, High-performance bulk thermoelectrics with all-scale hierarchical architectures, Nature, 489 (2012) 414-418.

[17] L.-D. Zhao, S.-H. Lo, Y. Zhang, H. Sun, G. Tan, C. Uher, C. Wolverton, V.P. Dravid, M.G. Kanatzidis, Ultralow thermal conductivity and high thermoelectric figure of merit in SnSe crystals, Nature, 508 (2014) 373-377.

[18] L.-D. Zhao, G. Tan, S. Hao, J. He, Y. Pei, H. Chi, H. Wang, S. Gong, H. Xu, V.P. Dravid, Ultrahigh power factor and thermoelectric performance in hole-doped single-crystal SnSe, Science, (2015) aad3749.

[19] M.S. Dresselhaus, G. Chen, M.Y. Tang, R. Yang, H. Lee, D. Wang, Z. Ren, J.P. Fleurial, P. Gogna, New directions for low-dimensional thermoelectric materials, Advanced Materials, 19 (2007) 1043-1053.

[20] C. Darwin, XCII. The reflexion of X-rays from imperfect crystals, The London, Edinburgh, and Dublin Philosophical Magazine and Journal of Science, 43 (1922) 800-829.

[21] F. Zwicky, Secondary structure and mosaic structure of crystals, Physical Review, 40 (1932) 63.

[22] H. Wang, W. Porter, H. Böttner, J. König, L. Chen, S. Bai, T. Tritt, A. Mayolett, J. Senawiratne, C. Smith, Thermoelectric Materials For Waste Heat Recovery: An International Collaboration For Transportation Applications, in, UT-Battelle: Oak Ridge National Laboratory, TN, 2012.

[23] D. Chakrabarti, D. Laughlin, The Cu-S (copper-sulfur) system, Bulletin of Alloy Phase Diagrams, 4 (1983) 254-271.

[24] K. Zhao, A.B. Blichfeld, E. Eikeland, P. Qiu, D. Ren, B.B. Iversen, X. Shi, L. Chen, Extremely Low Thermal Conductivity and High Thermoelectric Performance in Liquid-like $Cu_2Se_{1-x}S_x$ Polymorph Materials, Journal of materials Chemistry A, 5 (2017) 18148-18156.

[25] K. Zhao, P. Qiu, Q. Song, A.B. Blichfeld, E. Eikeland, D. Ren, B. Ge, B.B. Iversen, X. Shi, L. Chen, Ultrahigh thermoelectric performance in $Cu_{2-y}Se_{0.5}S_{0.5}$ liquid-like materials, Materials Today Physics, 1 (2017) 14-23.

[26] P. Qiu, Y. Zhu, Y. Qin, X. Shi, L. Chen, Electrical and thermal transports of binary copper sulfides CuxS with x from 1.8 to 1.96, APL Materials, 4 (2016) 104805.

[27] J. Yu, K. Zhao, P. Qiu, X. Shi, L. Chen, Thermoelectric properties of copper-deficient $Cu_{2-x}Se$ ($0.05 \leq x \leq 0.25$) binary compounds, Ceramics International, 43 (2017) 11142-11148.

[28] L. Yu, K. Luo, S. Chen, C.-G. Duan, Cu-deficiency induced structural transition of $Cu_{2-x}Te$, CrystEngComm, 17 (2015) 2878-2885.

[29] Y. He, T. Day, T. Zhang, H. Liu, X. Shi, L. Chen, G.J. Snyder, High Thermoelectric Performance in Non-Toxic Earth-Abundant Copper Sulfide, Advanced Materials, 26 (2014) 3974-3978.

[30] Y. He, T. Zhang, X. Shi, S.-H. Wei, L. Chen, High thermoelectric performance in copper telluride, NPG Asia Materials, 7 (2015) e210.

[31] A.F. May, E.S. Toberer, A. Saramat, G.J. Snyder, Characterization and analysis of thermoelectric transport in n-type $Ba_8Ga_{16-x}Ge_{30+x}$, Physical Review B, 80 (2009) 125205.

[32] H.J. Goldsmid, Introduction to thermoelectricity, Springer, 2010.

[33] S.V. Faleev, F. Léonard, Theory of enhancement of thermoelectric properties of materials with nanoinclusions, Physical Review B, 77 (2008) 214304.

[34] D.-K. Ko, Y. Kang, C.B. Murray, Enhanced thermopower via carrier energy filtering in solution-processable Pt–Sb2Te3 nanocomposites, Nano letters, 11 (2011) 2841-2844.

[35] J. Martin, L. Wang, L. Chen, G. Nolas, Enhanced Seebeck coefficient through energy-barrier scattering in PbTe nanocomposites, Physical review B, 79 (2009) 115311.

[36] A.F. May, J.-P. Fleurial, G.J. Snyder, Thermoelectric performance of lanthanum telluride produced via mechanical alloying, Physical Review B, 78 (2008).

[37] D. Cahill, S. Watson, R. Pohl, Lower limit to the thermal conductivity of disordered crystals, Physical Review B, 46 (1992) 6131-6140.
[38] W. Li, S. Lin, B. Ge, J. Yang, W. Zhang, Y. Pei, Low Sound Velocity Contributing to the High Thermoelectric Performance of Ag8SnSe6, Advanced Science, (2016) 1600196.
[39] K.S. Weldert, W.G. Zeier, T.W. Day, M. Panthofer, G.J. Snyder, W. Tremel, Thermoelectric transport in Cu7PSe6 with high copper ionic mobility, J Am Chem Soc, 136 (2014) 12035-12040.
[40] H. Liu, J. Yang, X. Shi, S.A. Danilkin, D. Yu, C. Wang, W. Zhang, L. Chen, Reduction of thermal conductivity by low energy multi-Einstein optic modes, Journal of Materiomics, 2 (2016) 187-195.
[41] T.M. Tritt, Thermal conductivity: theory, properties, and applications, Springer Science & Business Media, 2005.
[42] G.A. Slack, The thermal conductivity of nonmetallic crystals, Solid state physics, 34 (1979) 1-71.
[43] R.C. Zeller, R.O. Pohl, Thermal Conductivity and Specific Heat of Noncrystalline Solids, Physical Review B, 4 (1971) 2029-2041.
[44] D. Kapolnek, X.H. Wu, B. Heying, S. Keller, B.P. Keller, U.K. Mishra, S.P. DenBaars, J.S. Speck, Structural evolution in epitaxial metalorganic chemical vapor deposition grown GaN films on sapphire, Applied Physics Letters, 67 (1995) 1541-1543.
[45] V. Srikant, J.S. Speck, D.R. Clarke, Mosaic structure in epitaxial thin films having large lattice mismatch, Journal of Applied Physics, 82 (1997) 4286-4295.

Kunpeng Zhao is currently a Ph.D. candidate under the supervision of Prof. Lidong Chen and Xun Shi in Shanghai Institute of Ceramics, Chinese Academy of Sciences (SICCAS). He received his Bachelor's degree (2012) in Materials Science and Engineering from Xiamen University. His current research focuses on the design, fabrication, and tailoring of advanced thermoelectric materials.

Chenxi Zhu received his master degree from Shanghai Institute of Ceramics, Chinese Academy of

Sciences in 2017. He currently focuses on microstructural and in-situ study of thermoelectric materials through TEM techniques.

Pengfei Qiu obtained the Ph. D degree in Materials Chemistry and Physics from Shanghai Institute of Ceramics, Chinese Academy of Sciences in 2011 and Bachelor's degree BS in Materials science and Engineering from Wuhan University of Technology in 2006. Since 2013, he works in Shanghai Institute of Ceramics as an assistant and associated professor. His research interests are in advanced thermoelectric semiconductors, from synthesizing the materials to understanding the underlying physics and chemistry.

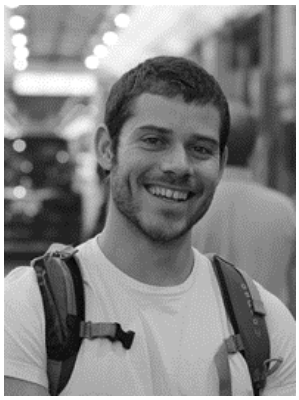

Anders Bank Blichfeld received his Ph. D degree in chemistry from Aarhus University in 2017. He is currently working at the Norwegian University of Science and Technology as a postdoc on the project 'From Aqueous Solutions to Oxide Thin Films and Hierarchical Structures'. His research interests mainly focus on the synthesis of thin films by chemical and physical deposition methods. In addition characterization by synchrotron in-situ X-ray diffraction techniques for example Rietveld refinement and pair distribution function (PDF) analyses.

Espen Eikeland is a consultant at the Danish Technological Institute, Centre for Nano Production and Micro Analysis. His main focus is on how the industry can benefit from the various advanced techniques found at Synchrotron and Neutron facilities. He received his Ph. D degree in Chemistry from Aarhus University in 2016. He is an experienced crystallographer in the field of single crystal high-pressure crystallography & material research in general. His work includes a wide variety of materials, from metal-organic frameworks, organic clathrates, CO_2 storage materials, to thermoelectrics and recently nanocatalyst materials for exhaust systems in motorcycles and passenger cars.

Dudi Ren is currently a Lab Manager in Thermoelectric Materials and Devices Laboratory of Shanghai Institute of Ceramics, Chinese Academy of Sciences (SICCAS). He specializes in the maintenance and operation of various instruments.

Bo Brummerstedt Iversen is professor of chemistry at Aarhus University (AU), Director of the Center for Materials Crystallography and the AU Center for Integrated Materials Research (iMAT). He is PhD from AU in 1995, and he holds both a Doctor of Science degree (AU, 2002) and a Doctor of Technology degree (DTU, 2010). He is a Fellow of the Royal Danish Academy of Science, and awards include the Queen Margrethe II Science Prize and the Danish Elite Researcher Award. He has been Knighted by Queen Margrethe II. Iversen has supervised 38 PhD degrees and published ~400 peer review papers.

Fangfang Xu received his B.S. at Tongji University in 1991. He obtained his Ph.D. degree in 1997 at Shanghai Institute of Ceramics, Chinese Academy of Sciences. He did postdoc research at CEA/France and NIMS/Japan during 1998-2004. He is now a professor in Shanghai Institute of Ceramics and currently his main research focuses on the structures and structure-property relationships of thermoelectric, ferroelectric and luminescence materials. So far he has published more than 150 papers.

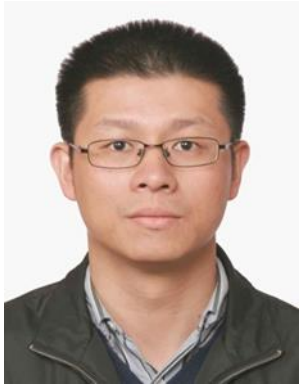

Xun Shi is a Professor in Shanghai Institute of Ceramics, Chinese Academy of Sciences (SICCAS), China. He received his B.S. (2000) in Tsinghua University and Ph.D. (2005) in the University of Chinese Academy of Sciences. He worked University of Michigan (USA) as a postdoctor from 2007 to 2009. Then he joined the R&D center in General Motors. At 2010, he came back SICCAS. His current research focuses on advanced thermoelectric materials. He has over 150 peer-reviewed publications 20 granted or submitted patents. His recent awards include National Science Fund for Distinguished Young Scholars (2016), National Science Fund of China for Excellent Young Scholars (2012), and Young Investigator Award, International Thermoelectric Society (2010).

Lidong Chen is a professor of Shanghai Institute of Ceramics, Chinese Academy of Sciences (SICCAS), and the Co-Editor-in-Chief of *npj Computational Materials*. He received his BS degree (1982) from Hunan University and doctor degree (1990) from Tohoku University. His research activity has majorly been focused on the design, synthesis and characterization of thermoelectric materials, as well as the integration of thermoelectric devices. He has published over 300 authored or co-authored papers in the area of inorganic materials and composites. He has received numerous awards including the research progress award of Japan Powder and Powder Metallurgy Society, GM Foundation Science & Technology Achievement Award (First Prize), State Science and Technology Awards of China.

Supplementary Material

High Thermoelectric Performance and Low Thermal Conductivity in $Cu_{2-y}S_{1/3}Se_{1/3}Te_{1/3}$ Liquid-like Materials with Nanoscale Mosaic Structures

Kunpeng Zhao[a,b], Chenxi Zhu[a,b], Pengfei Qiu[a], Anders Bank Blichfeld[c,d], Espen Eikeland[c,e], Dudi Ren[a], Bo Brummerstedt Iversen[c], Fangfang Xu[a], Xun Shi[a,*], and Lidong Chen[a,*]

Table S1. Crystallographic information for $Cu_2S_{1/3}Se_{1/3}Te_{1/3}$.

Sample	**$Cu_2S_{1/3}Se_{1/3}Te_{1/3}$**
Chemical formula[a]	$Cu_{2.1}S_{1/3}Se_{1/3}Te_{1/3}$
Space group	$P6_3/mmc$
Temperature / K	100
a / Å	4.052(2)
c / Å	6.849(6)
Volume / Å^3	97.54(12)
Z	2
ρ_{calc} / g/cm^3	7.264
μ / mm^{-1}	33.840
F(000)	190
$(\sin\theta/\lambda)_{max}$ / Å^{-1}	0.62
$N_{Tot,obs}$	884
$N_{Uniq,obs}$	52
$N_{Parameters}$	16
GOF	1.679
R_{int}	0.1054
R_1, $R_1[F^2>2\sigma(F^2)]$	0.110, 0100
wR_2, $wR_2[F^2>2\sigma(F^2)]$	0.332, 0.313
$\Delta\rho_{max}$, $\Delta\rho_{min}$ / e Å^{-3}	2.34, -1.03

[a] The partial atomic occupancies of Cu sites are free parameters in the structural model. Therefore, a slight deviation in the composition is obtained compared with the predicted formula.

Table S2. Percent atomic compositions of $Cu_2Se_{1/3}Se_{1/3}Te_{1/3}$ at ten randomly selected locations.

Elements	Atomic percent concentration										Average
Cu	66.11	66.88	66.53	66.64	66.48	66.38	65.80	65.90	66.15	66.30	66.317
S	11.43	11.14	11.42	11.35	11.52	11.55	11.45	11.54	11.42	11.54	11.436
Se	11.29	10.84	10.56	10.77	11.04	11.08	11.66	11.50	11.26	11.03	11.103
Te	11.17	11.14	11.49	11.25	10.96	10.99	11.09	11.06	11.17	11.14	11.146

Table S3. Percent atomic compositions of $Cu_{1.97}Se_{1/3}Se_{1/3}Te_{1/3}$ at ten randomly selected locations.

Elements	Atomic percent concentration										Average
Cu	66.17	66.43	66.32	66.06	66.11	66.12	66.13	66.14	66.45	66.15	66.208
S	11.34	11.3	11.23	11.44	11.45	11.34	11.28	11.34	11.21	11.29	11.322
Se	11.09	11.09	11.28	11.42	11.11	11.36	11.46	11.2	11.06	11.41	11.248
Te	11.4	11.18	11.17	11.08	11.33	11.18	11.13	11.32	11.28	11.15	11.222

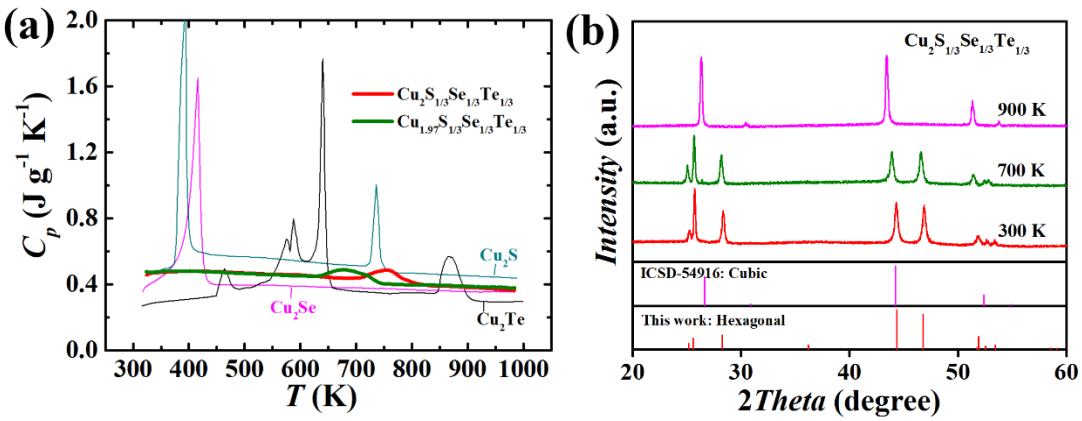

Figure S1. Temperature dependent heat capacity for $Cu_{2-y}S_{1/3}Se_{1/3}Te_{1/3}$ (y= 0, and 0.03) solid solutions. The data of Cu_2S, Cu_2Se and Cu_2Te matrix compounds are also included for comparison. **(b)** High temperature powder X-ray diffraction patterns for $Cu_2S_{1/3}Se_{1/3}Te_{1/3}$.

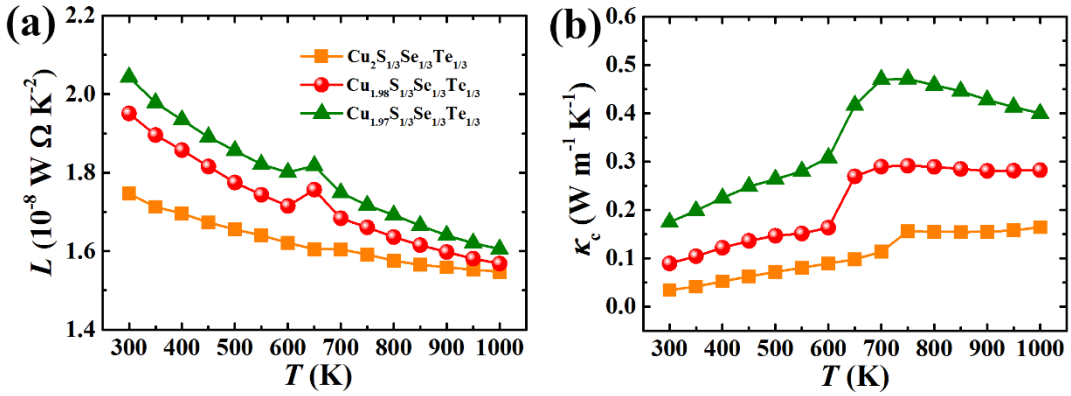

Figure S2. (a) Temperature dependent Lorenz number L and **(b)** carrier thermal conductivity κ_c for $Cu_{2-y}S_{1/3}Se_{1/3}Te_{1/3}$ (y= 0, 0.02, or 0.03) samples.

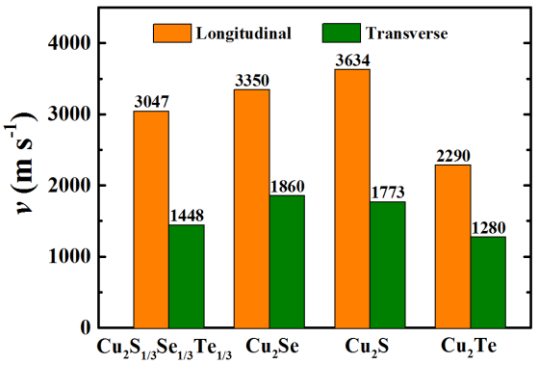

Figure S3. Longitudinal and transverse speeds of sound for $Cu_2S_{1/3}Se_{1/3}Te_{1/3}$, Cu_2S, Cu_2Se, and Cu_2Te at room temperature.

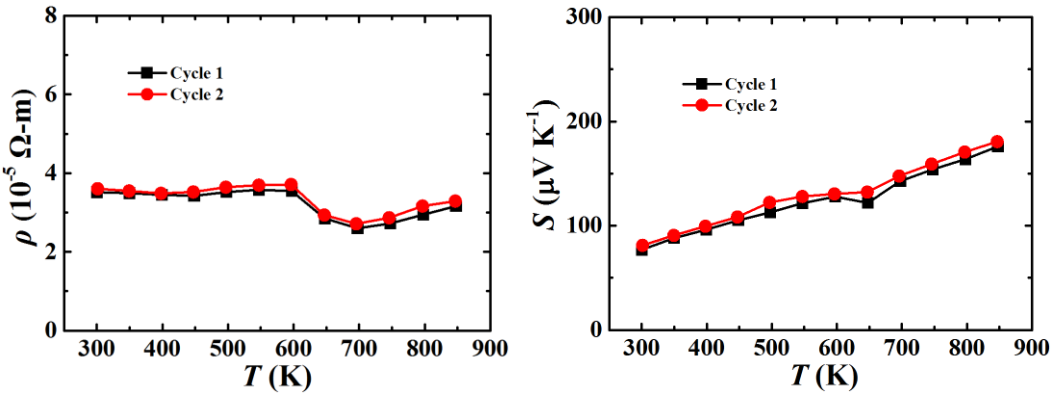

Figure S4. Repeatability test on electronic transport properties in $Cu_{1.97}Se_{1/3}Se_{1/3}Te_{1/3}$.